Journal of Fluids and Structures (2000) **14,** 157–182
doi: 10.1006/jfls.1999.0264, available online at http://www.idealibrary.com on IDEAL®

NUMERICAL SIMULATION OF LINEAR AND NONLINEAR DISTURBANCE EVOLUTION IN A BOUNDARY LAYER WITH COMPLIANT WALLS

O. Wiplier and U. Ehrenstein†

Université Lille 1, Laboratoire de Mécanique de Lille URA CNRS 1441, Bd. P. Langevin F-59655 Villeneuve d'Ascq Cedex, France

(Received 9 March 1998 and in final form 13 September 1999)

A computational method capable of simulating the spatial evolution of disturbances in a boundary-layer flow with compliant coatings has been developed. The flow geometry being an unknown of the problem, this difficulty is overcome by use of a mapping, the domain being fixed in the computational coordinates. The model takes into account the nonlinear fluid-structure interaction all over the flow field, as well as nonparallel effects due to the wall displacement and to the boundary-layer growth. First, the numerical solution procedure is tested by focusing on the linear and nonlinear spatial disturbance evolution for a spring-backed elastic plate which is only unstable with respect to Tollmien–Schlichting-type travelling waves. The numerical procedure is then used to study the influence of the initial disturbance amplitude on the disturbance development for a tensioned membrane. Finally, to simulate a true physical experiment, a spring-backed elastic plate of finite length is considered. It is shown that the numerical model is capable of detecting the interaction between Tollmien–Schlichting instabilities and flow-induced surface instabilities at the interface.

1. INTRODUCTION

The influence of compliant coatings on the transition in shear flows has extensively been studied since the pioneering experiments of Kramer (1960). Soon thereafter, it was recognized that compliant walls may be responsible for the occurrence of instability mechanisms other than the usual Tollmien–Schlichting waves which trigger the onset of transition in boundary-layer flow along rigid walls. The various instability modes due to the effect of wall compliance have originally been identified by Benjamin (1960). According to a classification scheme due to Carpenter & Garrad (1985, 1986), the instability waves are divided into fluid-based Tollmien–Schlichting instabilities and solid-based flow-induced surface instabilities. The latter are analogous to instabilities observed in hydro- and aeroelasticity. They consist of tavelling-wave flutter moving at speeds close to the solid free-wave speed, as well as static, divergence waves. Divergence waves have to be interpreted as an absolute instability, contrary to Tollmien–Schlichting instabilities and travelling-wave flutter which are convective instabilities. A thorough investigation of the influence of compliant coatings on Tollmien–Schlichting waves as well as the linear stability analysis of flow-induced surface instabilities has been performed by Carpenter & Garrad (1985, 1986). The problem of the proper choice of coating parameters capable of delaying spatial instabilities has been addressed by, among others, Joslin & Morris (1989). There is now clear evidence that,

†Present address: Université de Nice Sophia-Antipolis, Lab. J.-A. Dieudonné UMR CNRS 6621, Parc Valrose, F-06108 Nice Cedex 02, France

0889–9746/00/020157 + 26 $35.00/0

although compliant walls may have a favourable influence on instabilities triggered by Tollmien–Schlichting waves, for highly compliant walls travelling-wave flutter becomes dangerous. The state of the art at the late eighties has been documented by the surveys of Riley *et al.* (1988) and Carpenter (1990). An up-date of a review about boundary-layer interactions with compliant coatings (Gad-el-Hak 1986) has recently been published by Gad-al-Hak (1996). [Note that, in all the studies mentioned, the compliant wall acts as a passive device, whereas for instance Metcalfe *et al.* (1986) investigated the response of a laminar boundary-layer flow to active wall forcing for small wall amplitudes.]

Subsequent studies of compliant-wall/flow interaction confirmed that, while Tollmien–Schlichting waves may be suppressed using compliant coatings, hydroelastic instabilities may lead to flow breakdown. For instance, as shown by Lucey & Carpenter (1995) performing a linear stability analysis, the dramatic form of boundary-layer breakdown observed experimentally by Gaster (1987) was due to travelling-wave flutter. Recently, Davies & Carpenter (1997b) assessed the complex interaction between the various instability modes for a channel flow between compliant walls. Considering channel flow as a model problem for more general shear flows, Davies & Carpenter among others focus on the interaction between Tollmien–Schlichting modes and travelling-wave flutter modes. Those mode interactions can lead to absolute instability, contrary to the rigid case which is known to be convectively unstable (Deissler 1987). The problem of secondary instabilities of a boundary-layer flow with compliant coatings has been addressed by Joslin & Morris (1992), showing that secondary instability growth rates can be significantly reduced by use of compliant walls.

Plane channel flow has the advantage of being truly parallel, contrary to boundary-layer flow. Hence, some studies taking into account nonlinear effects in the presence of compliant walls focused on channel flow as a prototype for shear flows. Rotenberry (1992) and Ehrenstein & Rossi (1993) considered a quite simple wall governed by Hooke's law, computing nonlinear travelling waves of Tollmien–Schlichting type. For this perhaps oversimplified model it has been shown that finite-amplitude travelling waves may exist for parameter values where the basic state is linearly stable. These results are in qualitative agreement with the findings of Thomas (1992), based on an asymptotic triple-deck approach.

More recently, Ehrenstein & Rossi (1996) focused on nonlinear Tollmien–Schlichting waves for a Blasius flow over compliant coatings, using the locally parallel flow approximation. It was shown numerically that for a specific class of compliant coatings, modelled as tensioned membranes, the nonlinear bifurcation behaviour becomes highly subcritical. However, for these computations the shortcomings of the underlying parallel-flow assumption became evident by considering highly flexible walls. In that case the computed mean-flow distortions appeared to be erroneous, which was attributed by Ehrenstein & Rossi to nonparallel effects. The influence of boundary-layer growth on the linear stability in the presence of compliant coatings has been addressed by Yeo *et al.* (1994), using a multiple-scale analysis. According to these results, the nonparallelism has an overall destabilizing influence on the Tollmien–Schlichting instabilities as well as on travelling-wave flutter, in particular for low Reynolds numbers.

An alternative way for including nonparallel effects would be to perform a direct numerical simulation of the spatial disturbance evolution. Recently, numerical simulations of the linear evolution of disturbance waves in a channel, the lower wall being covered with a compliant panel of finite length, have been performed by Davies & Carpenter (1997a). The response of compliant walls to uniform flow has recently been studied by Lucey *et al.* (1997a) using a nonlinear model for the wall mechanics. The fluid perturbation pressure is evaluated assuming unsteady potential flow, and it is shown that the fluid-structure interaction may lead to the appearance of nonlinear divergence waves. Computations of

complex interactions between a boundary layer and a compliant wall, the rotational flow component being obtained by a discrete-vortex method, have been published by Lucey *et al.* (1997b).

The aim of the present study is to perform a direct numerical simulation of the nonlinear fluid-structure interaction by solving the Navier–Stokes equations coupled to the wall model. The numerical simulation of spatial disturbance growth in the presence of compliant walls is a challenging problem, the geometry of the flow being part of the solution. The problem of direct numerical simulation of flow with complex, time-dependent wall geometries, has been addressed for instance by Carlson *et al.* (1995). In the present study, we present a numerical procedure capable of describing the spatial, nonparallel evolution of disturbance growth in a boundary layer coupled to a flexible wall. The model takes into account the full nonlinear interaction between the fluid and the structure. The wall is covered with a spring-backed elastic plate or a tensioned membrane similar to flexible wall models used by other investigators.

The paper is organized as follows. In Section 2, the governing equations and the numerical simulation procedure are outlined. Numerical experiments are presented in Section 3. The solution procedure is tested and different types of compliant coatings are considered including the case of a finite-length panel. Finally, Section 4 is devoted to a summary of the results.

2. GOVERNING EQUATIONS AND SOLUTION PROCEDURE

2.1. Wall Model and Basic State

The compliant wall is modelled as a spring-backed elastic plate, or alternatively as a tensioned membrane with damping, where only vertical displacements are allowed. Similar compliant coatings have been considered in previous works and they are generally believed to be representative models for the study of passive transition control using flexible walls. Furthermore, the onset of transition in boundary-layer flows being triggered by two-dimensional Tollmien–Schlichting waves, we limit the scope of the present study to two-dimensional disturbances and we emphasize the fluid-structure interaction.

We consider an incompressible fluid flow of viscosity ν^* past a plane wall, which in the rigid case is located at $y^* = 0$, $0 \leq x^*$. The basic state is a boundary-layer flow in the absence of a pressure gradient and hence the interface remains flat. The basic state $(U^*(x^*, y^*), V^*(x^*, y^*))$ is a solution of the boundary-layer equations along a flat plate. The computational domain in the streamwise direction is $x_a^* \leq x^* \leq x_b^*$. The velocity at infinity U_∞^* is used as reference velocity and the displacement thickness $\delta_a^* = \gamma\sqrt{\nu^* x_a^*/U_\infty^*}$, $\gamma = 1{\cdot}7208$, at in-flow is the reference length. It is convenient to use the similarity formulation for the stream function $\psi^* = \sqrt{\nu^* U_\infty^* x^*} f(y_x)$, with $y_x = y^*/\sqrt{\nu^* x_a^*/U_\infty^*}$, f being the solution of the Blasius equation [cf. Schlichting (1979)], to determine the nondimensional, nonparallel basic flow at $x_a \leq x \leq x_b$, $0 \leq y < \infty$ (the stars are dropped for the dimensionless variables). The Reynolds number is defined with the displacement thickness at in-flow

$$\mathrm{Re} = \frac{U_\infty^* \delta_a^*}{\nu^*}. \tag{1}$$

When the wall is compliant the dimensionless vertical displacement $\eta(x, t)$ is a solution of the dynamical equation

$$m\frac{\partial^2 \eta}{\partial t^2} + d\frac{\partial \eta}{\partial t} + B\frac{\partial^4 \eta}{\partial x^4} - T\frac{\partial^2 \eta}{\partial x^2} + \kappa\eta = [-p + \sigma](x, \eta). \tag{2a}$$

Here p is the dimensionless perturbation fluid pressure and σ is the normal viscous stress of the perturbation fluid velocity, with

$$\sigma = \frac{2}{\mathrm{Re}}\left(\frac{\partial u}{\partial x}n_1^2 + \left(\frac{\partial u}{\partial y} + \frac{\partial v}{\partial x}\right)n_1 n_2 + \frac{\partial v}{\partial y}n_2^2\right), \tag{2b}$$

(u, v) being, respectively, the streamwise and the wall-normal component of the disturbance flow velocity and $\mathbf{n} = (n_1, n_2) = (1/\sqrt{1 + (\partial\eta/\partial x)^2}(-\partial\eta/\partial x, 1)$ is the unit normal vector at the wall. The dimensionless coating parameters are such that

$$m = \frac{m^*}{\delta_a^* \rho^*}, \quad d = \frac{d^*}{U_\infty^* \rho^*}, \quad B = \frac{B^*}{\delta_a^{*3} \rho^* U_\infty^{*2}}, \quad T = \frac{T^*}{\delta_a^* \rho^* U_\infty^{*2}}, \quad \kappa = \frac{\kappa^* \delta_a^*}{\rho^* U_\infty^{*2}}, \tag{2c}$$

the coating characteristics m^*, d^*, B^*, T^* and κ^* being, respectively, the mass density per unit length, damping, flexural rigidity of the plate, tension, and spring stiffness. As usual the pressure is made dimensionless using $\rho^* U_\infty^{*2}$, ρ^* being the fluid density. The total fluid flow is governed by the Navier–Stokes system which has to be solved in the (unknown) domain

$$x_a \le x \le x_b, \qquad \eta(x, t) \le y \le \infty. \tag{3}$$

Only vertical displacements are allowed, hence the kinematical condition at the moving boundary may be expressed as

$$(U + u)[x, \eta(x, t)] = 0, \qquad \frac{\partial n}{\partial t} = (V + v)[x, \eta(x, t)]. \tag{4}$$

2.2. The Numerical Solution Procedure

The geometry being an unknown of our problem, we transform the physical domain (3) into a computational fixed domain, using the mapping

$$t' = t, \qquad x' = x, \qquad y' = y - \eta(x, t). \tag{5a}$$

Using equation (5a) the divergence operator, the Laplacian and the time derivative become

$$\boldsymbol{\nabla} = \boldsymbol{\nabla}' + \mathbf{D}(\eta), \qquad \Delta = \Delta' + L(\eta), \qquad \frac{\partial}{\partial t} = \frac{\partial}{\partial t'} + D_t(\eta), \tag{5b}$$

with

$$\mathbf{D}(\eta) = \left(-\frac{\partial \eta}{\partial x'}\frac{\partial}{\partial y'}, 0\right), \quad D_t(\eta) = -\frac{\partial \eta}{\partial t'}\frac{\partial}{\partial y'} \quad \text{and}$$

$$L(\eta) = -\frac{\partial^2 \eta}{\partial x'^2}\frac{\partial}{\partial y'} - 2\frac{\partial \eta}{\partial x'}\frac{\partial^2}{\partial x' \partial y'} + \left(\frac{\partial \eta}{\partial x'}\right)^2 \frac{\partial^2}{\partial y'^2}.$$

The Navier–Stokes system may be written in terms of the disturbance flow velocity $\mathbf{u}$ and the disturbance pressure p as

$$\frac{\partial \mathbf{u}}{\partial t'} + G(\mathbf{u}) + N(\mathbf{u}) - \frac{1}{\mathrm{Re}}\Delta' \mathbf{u} + \boldsymbol{\nabla}' p = -GL(\eta) - GL(\eta, \mathbf{u}) - G(\eta, p) - N(\eta, \mathbf{u}), \tag{6a}$$

$$\boldsymbol{\nabla} \cdot \mathbf{u} = -\mathbf{D}(\eta) \cdot \mathbf{U} - \mathbf{D}(\eta) \cdot \mathbf{u}, \tag{6b}$$

where the gradient term $G(\mathbf{u})$ and the convective term $N(\mathbf{u})$ are $G(\mathbf{u}) = (\mathbf{U}\cdot\nabla')\mathbf{u} + (\mathbf{u}\cdot\nabla')\mathbf{U}$ and $N(\mathbf{u}) = (\mathbf{u}\cdot\nabla')\mathbf{u}$. Although the basis flow $\mathbf{U}$ is solution of the boundary-layer equations only, we have assumed that $\mathbf{U}$ is a solution of the above Navier–Stokes system in the flat case ($\eta \equiv 0$), according to order-of-magnitude analysis (Joslin *et al.* 1993). In the compliant case, extra terms arise in the right-hand side of equations (6a), as a consequence of the mapping, with

$$GL(\eta) = D_t(\eta)\mathbf{U} + (\mathbf{U}\cdot\mathbf{D}(\eta))\mathbf{U} - \frac{1}{\mathrm{Re}}L(\eta)\mathbf{U} \tag{6c}$$

depending on the unknown η only, whereas

$$GL(\eta, \mathbf{u}) = D_t(\eta)\mathbf{u} + (\mathbf{U}\cdot\mathbf{D}(\eta))\mathbf{u} + (\mathbf{u}\cdot\mathbf{D}(\eta))\mathbf{U} - \frac{1}{\mathrm{Re}}L(\eta)\mathbf{u} \tag{6d}$$

involves products of η and $\mathbf{u}$. Finally the non-Cartesian part of the convective term and the pressure gradient are

$$N(\eta, \mathbf{u}) = (\mathbf{u}\cdot\mathbf{D}(\eta))\mathbf{u}, \quad G(\eta, p) = \mathbf{D}(\eta)p. \tag{6e}$$

In the computational frame (x', y'), the kinematical conditions (4) and the boundary conditions at infinity for the disturbance velocity field are

$$u(x', 0) = 0, \quad \frac{\partial\eta}{\partial t'} = v(x', 0) \quad \text{and} \quad p, u, v \to 0 \text{ as } y' \to \infty. \tag{7}$$

For the transformed system, the dynamical equation (2a) is written at the fixed boundary $y' = 0$, the normal viscous stress (2b) being transformed by equation (5a).

Using the identity in the physical frame of coordinates

$$\nabla\cdot((\nabla\cdot\mathbf{u}_t)\mathbf{u}_t) = (\nabla\cdot\mathbf{u}_t)^2 + (\mathbf{u}_t\cdot\nabla)(\nabla\cdot\mathbf{u}_t) + 2J(u_t, v_t), \tag{8a}$$

with

$$J(u_t, v_t) = \frac{\partial u_t}{\partial y}\frac{\partial v_t}{\partial x} - \frac{\partial u_t}{\partial x}\frac{\partial v_t}{\partial y}, \tag{8b}$$

$\mathbf{u}_t = (u_t, v_t) = (u + U, v + V)$ being the total velocity field; also, taking the divergence of the momentum equations of the Navier–Stokes system, one gets for the total fluid pressure

$$\Delta p_t = -2J(u_t, v_t) \tag{8c}$$

for incompressible flow with $\nabla\cdot\mathbf{u}_t = 0$. Consequently, the Poisson equation for the disturbance pressure in the transformed coordinates becomes

$$\Delta' p = -L(\eta)p - 2J'(u, v), \tag{9}$$

with $J'(u, v) = J(u + U, v + V) - J(U, V)$.

For time-integration of (6a), second-order backward Euler differencing is used; the Cartesian part of the Laplacian as well as the pressure gradient are taken implicitly. An explicit second-order Adams-Bashforth scheme is used for the remaining terms. The discrete version of equations (6a, b) is

$$(\Delta' - 3\tau)\mathbf{u}^{n+1} = \nabla' q^{n+1} + \phi\{-4\tau\mathbf{u}^n + \tau\mathbf{u}^{n-1} + \mathrm{Re}[G(\mathbf{u}) + N(\mathbf{u})]^{n,n-1}\}$$
$$+ \mathrm{Re}\,\phi[GL(\eta) + GL(\eta, \mathbf{u}) + G(\eta, p) + N(\eta, \mathbf{u})]^{n,n-1}, \tag{10a}$$

$$\nabla\cdot\mathbf{u}^{n+1} = -\phi[\mathbf{D}(\eta)\cdot\mathbf{U} + \mathbf{D}(\eta)\cdot\mathbf{u}]^{n,n-1}. \tag{10b}$$

The superscript $(n, n-1)$ means an explicit Adams–Bashforth differencing with $[\ ]^{n,n-1} = 2[\ ]^n - [\ ]^{n-1}$. Here $\tau = \mathrm{Re}/2\Delta t$, Δt being the time-step and $q = \mathrm{Re}\, p$. In order to avoid reflections at the out-flow boundary, a buffer domain technique is used [cf. Streett & Macaraeg (1989)]. For this purpose, a buffer domain in inserted between the physical domain and the out-flow boundary. The gradient and convective terms as well as those depending on η in equation (10) are multiplied by an attenuation function ϕ with $\phi = 1$ in the physical domain of interest and rapidly decreasing to zero in the buffer domain. Thus, system (10) is progressively transformed into a linear Stokes-type problem for a Cartesian geometry in the buffer domain and the instability is smoothed out. The discrete version of the pressure equation (9) is $(q = \mathrm{Re}\, p)$

$$\Delta' q^{n+1} = -\,\mathrm{Re}\,\phi[L(\eta)p + 2J'(u, v)]^{n,n-1}. \tag{11}$$

Equation (11) is the Poisson equation for the perturbation pressure, assuming incompressibility $\nabla \cdot \mathbf{u}_t = 0$ for the total fluid velocity. Reciprocally, let us assume that, during the time-marching algorithm, $\nabla \cdot \mathbf{u}_t = 0$ at previous time-steps $n, n-1$. Taking the divergence of the discretized momentum equation together with equation (11), one gets a homogeneous (up to second-order in time) Helmholtz equation for $(\nabla \cdot \mathbf{u}_t)^{n+1}$. It is hence sufficient to annihilate $(\nabla \cdot \mathbf{u}_t)^{n+1}$ on the boundary Γ that is up to second-order in time

$$\nabla' \cdot \mathbf{u}_{|\Gamma}^{n+1} = -\,\phi[\mathbf{D}(\eta) \cdot \mathbf{U} + \mathbf{D}(\eta) \cdot \mathbf{u}]_{|\Gamma}^{n,n-1} \tag{12}$$

to recover a divergence-free velocity field at the actual time step $n+1$. Consequently, for a reasonably divergence-free initial condition, the incompressibility condition will be satisfied with the same order of accuracy as that of the time-marching algorithm.

The time-differencing of the kinematical condition (7) leads to

$$u^{n+1}(x', 0) = 0; \quad v^{n+1}(x', 0) = \frac{3\eta^{n+1} - 4\eta^n + \eta^{n-1}}{2\Delta t}. \tag{13}$$

The discrete version of the dynamical equation, using second-order backward differencing in time, is

$$m\,\frac{2\eta^{n+1} - 5\eta^n + 4\eta^{n-1} - \eta^{n-2}}{\Delta t^2} + d\,\frac{3\eta^{n+1} - 4\eta^n + \eta^{n-1}}{2\Delta t}$$

$$+ B\,\frac{\partial^4 \eta^{n+1}}{\partial x'^4} - T\,\frac{\partial^2 \eta^{n+1}}{\partial x'^2} + \kappa\eta^{n+1} = \phi\{-p^{n+1} + \sigma^{n,n-1}\}(x', 0). \tag{14}$$

Here the pressure term is taken implicitly, and the Adams–Bashforth scheme is used for the normal viscous stress. Again, we multiply the forcing term by the attenuation function ϕ, consequently the displacement η will tend to zero in the buffer domain. To equation (14) we have to add the boundary conditions for η which will be discussed in Section 3. The algorithm to solve equations (10)–(12) coupled to (13) and (14) is described in the Appendix and it is based on the influence matrix technique used to recover a boundary condition for the pressure equivalent to equation (12).

For the space discretization, fourth-order central finite differences are used for the second derivatives in the steamwise x'-direction, except at boundary and near-boundary nodes where fourth-order forward or backward differences are used. In order to avoid oscillations, we use eighth-order finite differences for the first derivatives in x' as recommended by Rist & Fasel (1995) for the simulation of transition in the flat-plate case. The attenuation function ϕ is the same as in Joslin *et al.* (1992, 1993).

Chebyshev collocation is used in the wall-normal y'-direction. We map the unbounded domain $0 \le y' < \infty$ on a finite domain $\xi \in [-1, 1]$, using the algebraic transformation

$$y' = \frac{y_{\max} L(1+\xi)}{2L + y_{\max}(1-\xi)}, \quad \text{the collocation points being } \xi_j = \cos(j\pi/K), \quad 0 \le j \le K. \tag{15}$$

In fact, the domain y' is truncated at $0 \le y' \le y_{\max}$ (typically $y_{\max} \ge 75$ and $L \approx 1$) as in Joslin *et al.* (1992). The y'-derivatives are computed by means of the collocation matrix method [cf. Canuto *et al.* 1987)]. For the inversion of the discrete Helmholtz- and Poisson-like equations we use the eigenvalue decomposition method. (The problem, once the discrete second-derivative operator in y' diagonalized, is transformed into a series of one-dimensional Helmholtz-like equations in x', which can be solved efficiently using the pentadiagonal structure of the matrices.)

3. NUMERICAL RESULTS

Linear spatial stability results are used to prescribe a disturbance-forcing function at in-flow x_a whereas at out-flow, the disturbance being smoothed out in the buffer domain, the perturbation is set to zero. First, we briefly discuss some linear stability results. Then, the numerical solution procedure is tested, before some numerical experiments are performed for a tensioned membrane and a spring-backed elastic plate.

3.1. Linear Stability Revisited

The linear stability of a boundary-layer flow with compliant coatings has extensively been studied for different classes of flexible surfaces. Here, linear stability analyses, based on the parallel-flow assumption for the basic flow $\mathbf{U} = (U(y), 0)$, provide the in-flow conditions for the nonparallel spatial simulation of the disturbance development.
Linearizing equations (6a, b) one gets

$$\frac{\partial \mathbf{u}}{\partial t'} + U(y')\frac{\partial \mathbf{u}}{\partial x'} + v\frac{\mathrm{d}U}{\mathrm{d}y'}(y')\mathbf{i} - \frac{1}{\mathrm{Re}}\Delta'\mathbf{u} + \nabla' p$$
$$= \left[\frac{\partial \eta}{\partial t'}\frac{\mathrm{d}U}{\mathrm{d}y'}(y') + U(y')\frac{\partial \eta}{\partial x'}\frac{\mathrm{d}U}{\mathrm{d}y'}(y') - \frac{1}{\mathrm{Re}}\frac{\partial^2 \eta}{\partial x'^2}\frac{\mathrm{d}U}{\mathrm{d}y'}(y')\right]\mathbf{i}, \tag{16a}$$

$$\nabla' \cdot \mathbf{u} = \frac{\partial \eta}{\partial x'}\frac{\mathrm{d}U}{\mathrm{d}y'}(y'), \tag{16b}$$

$\mathbf{i}$ being the unit vector in the streamwise x'-direction, and $U(y')$ being the Blasius profile.

In most of the studies on linear stability no mapping is performed in the linearized Navier–Stokes system [which then reduces to the left-hand side of equations (16a, b)]. Rather than performing the coordinate transformation, the kinematical conditions $u_t(x, \eta) = 0$, $\partial\eta/\partial t = v_t(x, \eta)$ for the total flow velocity are expanded in a Taylor series, and after linearization

$$\tilde{u}(x, 0) + \eta\frac{\mathrm{d}U}{\mathrm{d}y}(0) = 0, \quad \frac{\partial \eta}{\partial t} = \tilde{v}(x, 0), \tag{17}$$

$(\tilde{u}, \tilde{v})$ being the perturbation velocity, solution of the linearized Navier–Stokes system in Cartesian coordinates. One may wonder if the two approaches are equivalent, that is, by

comparing both incompressibility conditions, if one may write $u = \tilde{u} + \eta[\mathrm{d}U(y)/\mathrm{d}y]$ and $v = \tilde{v}$. Injecting this expression into equation (16a) one gets

$$\mathrm{NS}\begin{pmatrix}\tilde{u}\\ \tilde{v}\end{pmatrix} = \frac{1}{\mathrm{Re}}\,\eta\,\frac{\mathrm{d}^3 U}{\mathrm{d}y^3}\,(y)\mathbf{i}, \tag{18}$$

where $\mathrm{NS}(\begin{smallmatrix}\tilde{u}\\ \tilde{v}\end{smallmatrix})$ stands for the linearized Navier–Stokes system in Cartesian coordinates. While the extra term on the right-hand side in equation (18) will be small for moderately flexible walls, it may become nonnegligible for large wall displacements which occur for instance when travelling-wave flutter is present. In the following, we shall qualify as Cartesian formulation (CF) the system (18) without the right-hand side, the system being in that case equivalent to the Orr–Sommerfeld equation once the solution is written as normal modes, coupled to the kinematical condition (17) and the dynamical equation (2) (the normal viscous stress being linearized). The system (16) will be called the non-Cartesian formulation (NCF).

For the standard normal-mode analysis, writing

$$\mathbf{u} = (\hat{u}(y), \hat{v}(y))\ \mathrm{e}^{\mathrm{i}(\alpha x - \omega t)}, \quad p = \hat{p}(y)\mathrm{e}^{\mathrm{i}(\alpha x - \omega t)}, \quad \eta = \hat{\eta}\mathrm{e}^{\mathrm{i}(\alpha x - \omega t)}, \tag{19}$$

leads to an eigenvalue problem for the complex temporal eigenvalue ω as function of the wavenumber α and the Reynolds number Re, which is solved by standard QZ-algorithms, once the modes have been discretized by Chebyshev collocation. To compare both the CF- and NCF-results, an example of Carpenter & Gajjar (1990) is considered as a test case. The modal is that of a Kramer-type wall, where a flexible thin plate is supported by springs. The elastic modulus is $E = 0{\cdot}5\ \mathrm{MN/m^2}$, the plate density $\rho_m = 946\ \mathrm{kg/m^3}$, the plate thickness $b = 2\ \mathrm{mm}$ and the spring stiffness $\kappa^* = 115\ \mathrm{MN/m^3}$. The coefficients in equation (2c) are $m^* = b\rho_m$, $B^* = Eb^3/[12(1 - \nu_p^2)]$, with $\nu_p = 0{\cdot}5$ ($d^* = T^* \equiv 0$). The fluid is water with $U_\infty^* = 18\ \mathrm{m/s}$, $\rho^* = 1025\ \mathrm{kg/m^3}$ and $\nu^* = 1{\cdot}37 \times 10^{-6}\ \mathrm{m^2/s}$.

The computations have been performed at $\mathrm{Re}_\delta = 2000$, the Reynolds number being formed with the boundary-layer displacement thickness. Focusing on *temporally growing* travelling-wave flutter instabilities, the complex wave speed $c = \omega/\alpha = c_r + \mathrm{i}c_i$ has been computed as function of the wavenumber α. The results are depicted in Figure 1, the solid line being the real part c_r. The dotted line corresponds to values of $100c_i$ for the CF-approach, whereas the broken line represents the amplification rates obtained using the transformed NCF system. Concerning the real part c_r, the two approaches are identical. However, there are differences for the amplification rate c_i in Figure 1. Indeed the CF computations predict an instability (for $c_i > 0$) at low wavenumbers α, where $c_r > 1$. This is identical to the CF results published by Carpenter & Gajjar (1990) (those instabilities with a wave speed $c_r > 1$ have been considered as unphysical by these authors). However, this instability disappears when the NCF-approach is used for the stability computations.

Besides a numerical CF-analysis, Carpenter & Gajjar (1990) also performed an asymptotic analysis including nonparallel effects due to the wall displacement. It appears that our NCF-computations shown in Figure 1 are almost identical to those shown in Carpenter & Gajjar (1990, Figure 9) using the asymptotic approach. The differences between the CF- and NCF-computations may also be seen by inspecting the eigenfunctions. For $\alpha = 0{\cdot}11$, Figure 2 shows the quantity $(U - c_r)\hat{v}_i$, $\hat{v}_i$ being the imaginary part of the wall-normal mode (the latter one being normalized such that $\hat{v} = 1$ at the wall). Again, the influence of the nonparallel terms due to η is evident; the solid-line profile corresponds to the CF-system and the broken line to the NCF-approach. Also [cf. Carpenter & Gajjar (1990, Figure 10)], our computations with system (16) are close to the asymptotic analysis of Carpenter & Gajjar. Note that for the CF-type computations for $\alpha = 0{\cdot}11$, $c = 0{\cdot}828 + \mathrm{i}0{\cdot}00307$

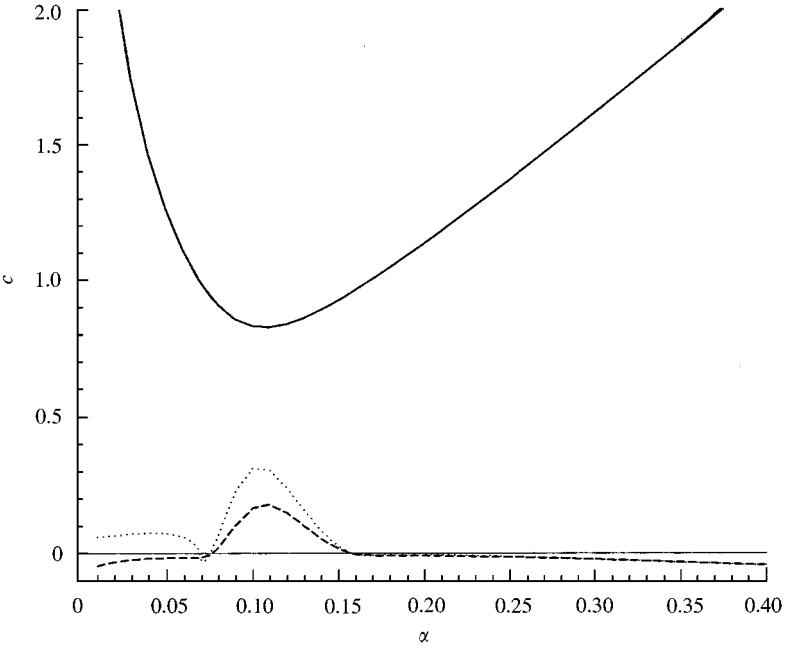

Figure 1. Complex wavespeed $c = c_r + \mathrm{i}c_i$ for TWF instability, spring-backed flexible plate with $b = 2$ mm, $E = 0{\cdot}5$ MN/m^2 and $\kappa^* = 115$ MN/m^3; —, c_r; – – –, $100c_i$ with transformed NCF-system; ⋯, $100c_i$ with CF-system.

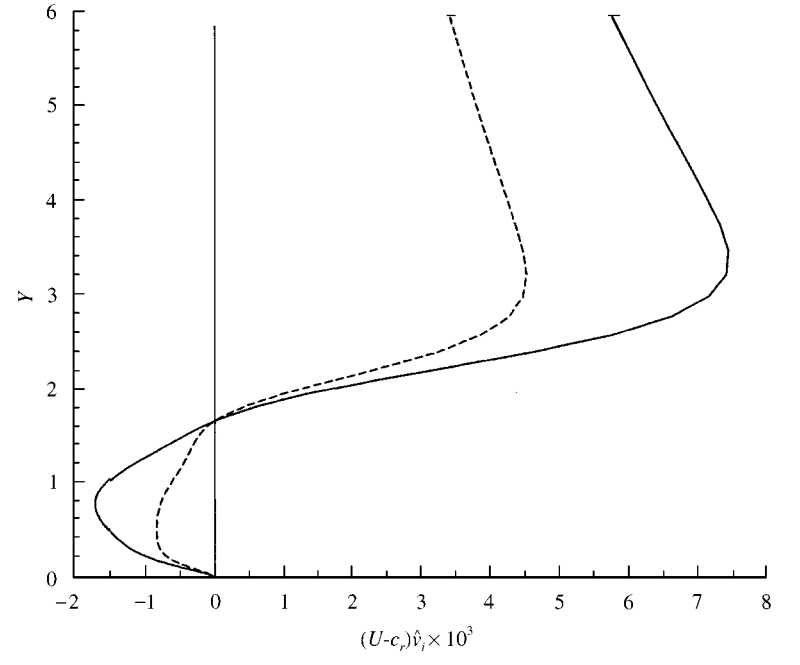

Figure 2. Profile of $(U - c_r)\hat{v}_i$ with $\hat{v} = \hat{v}_r + \mathrm{i}\hat{v}_i$ the TWF instability wall-normal mode, for the same parameter values as in Figure 1: —, CF-approach; – – –, NCF-approach.

(identical with the results of Carpenter & Gajjar for their CF-computations), whereas for the NCF-approach one gets $c = 0{\cdot}829 + \mathrm{i}0{\cdot}00179$, which again illustrates the influence of nonparallel effects due to the wall displacement on the amplification rate c_i.

3.2. Validation of Simulation Procedure

The *spatial* stability results for real frequencies ω and complex wavenumbers α are used to prescribe the time-periodic perturbation at in-flow x_a. These computations have been performed using the linearized Navier–Stokes system (16) with equation (19) (coupled to the kinematical condition and to the dynamical equation). The wavenumber appears as squared quantity in the stability equations, and a generalized eigenvalue problem for α can be recovered by introducing extra variables.

Writing the stability mode as $\hat{\mathbf{u}}(y)\mathrm{e}^{\mathrm{i}(\alpha(x-x_a)-\omega_0 t]}$ (with $\hat{\mathbf{u}}(y) = \hat{\mathbf{u}}_r(y) + \mathrm{i}\hat{\mathbf{u}}_i(y)$), the real time-dependent in-flow perturbation is

$$\mathbf{\Phi}(y, t) = \hat{\mathbf{u}}_r(y)\cos(\omega_0 t) + \hat{\mathbf{u}}_i(y)\sin(\omega_0 t), \quad \text{with } \operatorname*{Max}_y \sqrt{\hat{u}_r(y)^2 + \hat{u}_i(y)^2} = A, \tag{20}$$

A being a given amplitude and $\hat{u}(y)$ the steamwise component of the eigenmode. In order to test our numerical solution procedure, we consider as a first test-case a spring-backed elastic plate [$T = d = 0$ in equation (2a)] with a (perhaps unrealistic) plate thickness of $b = 10^{-1}$ mm; the elastic modulus is $E = 0{\cdot}5\ \mathrm{MN/m^2}$ and the spring stiffness is $\kappa^* = 10^4\ \mathrm{MN/m^3}$ (with a plate density of $\rho_m = 946\ \mathrm{kg/m^3}$, the fluid being water with $U_\infty^* = 18$ m/s, $\rho^* = 1025\ \mathrm{kg/m^3}$ and $\nu^* = 1{\cdot}37 \times 10^{-6}\ \mathrm{m^2/s}$). Here the spring stiffness is sufficiently high to suppress travelling-wave flutter and the plate is sufficiently thin for the flexibility to have an influence on linear stability. Spatial linear stability results are depicted in Figure 3; the broken line corresponds to the compliant case and the linear stability results for a rigid plate are shown as well.

In order to compare the nonparallel spatial stability computations to linear stability results based on the locally parallel flow assumption, we first simulate the spatial development of disturbances using the *linearized* Navier–Stokes system. The computational domain is sketched in Figure 4. The dimensional frequency at inflow is $\omega_0^* = \omega_0 U_\infty^*/\delta_a^*$; the spatial stability results in Figure 3 are based on the locally parallel flow assumption, hence the dimensionless frequency is $\omega = \omega_0^*\delta^*/U_\infty^* = \omega_0^*\nu^*\mathrm{Re}_\delta/U_\infty^{*2}$. The Reynolds number (1) based on the displacement thickness depends on x^*, and consequently, prescribing a frequency ω_0 at in-flow x_a, the spatial evolution in the streamwise direction corresponds to a displacement along the dotted line passing through (0, 0) and (Re, ω_0) on the linear stability diagram. In Figure 3, the in-flow corresponds to the point marked at Re = 600 and $\omega_0 = 0{\cdot}08$, the second point at Re = 1100 on the dotted line corresponds to the end of the physical domain (the buffer domain starts here). [A second line passing through (Re = 688·315, $\omega_0 = 0{\cdot}05921$) corresponds to a rigid-wall case simulation to be discussed later in this section].

The linear amplitude growth, from in-flow x_a^* to a location x^* on the wall, resulting from stability computations based on the locally parallel flow assumption, is given by

$$\frac{A}{A_0} = \exp\left(-\int_{x_a^*}^{x^*} \alpha_i^*\, \mathrm{d}x^* \right),$$

$-\alpha_i^*$ being the local dimensional spatial growth factor predicted by the linear stability theory and A_0 is the amplitude at in-flow. For the spatial numerical simulation, the in-flow perturbation being time-periodic with periodicity $\Lambda = 2\pi/\omega_0$, the velocity components may

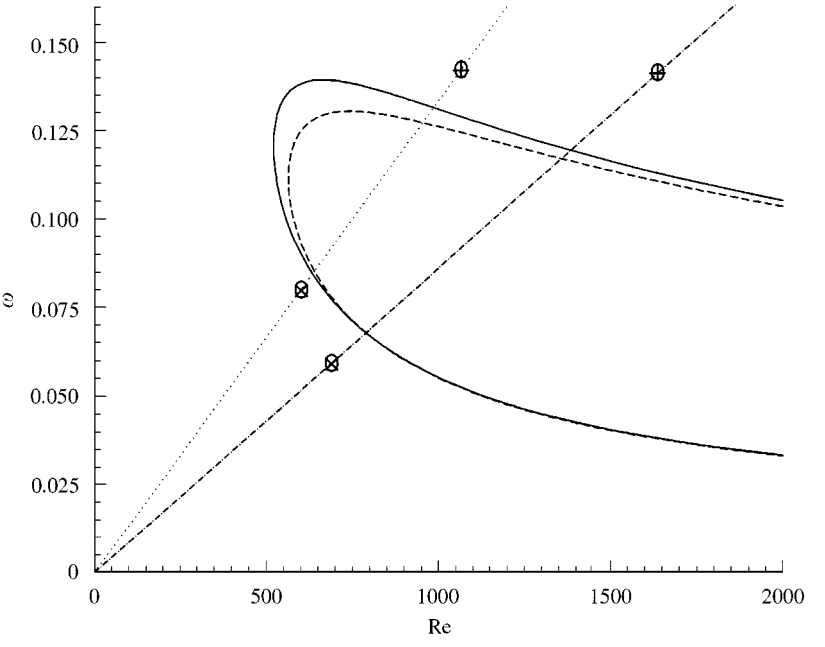

Figure 3. Neutral curves for spatial instability: —, rigid case; – – –, spring-backed elastic plate with $b = 0{\cdot}1$ mm, $E = 0{\cdot}5$ MN/m^2 and $\kappa^* = 10^4$ MN/m^3. Spatial numerical computations correspond to displacement along: ....., compliant case; –·–·–, rigid case. ⊗ marks in-flow and out-flow of computational domain.

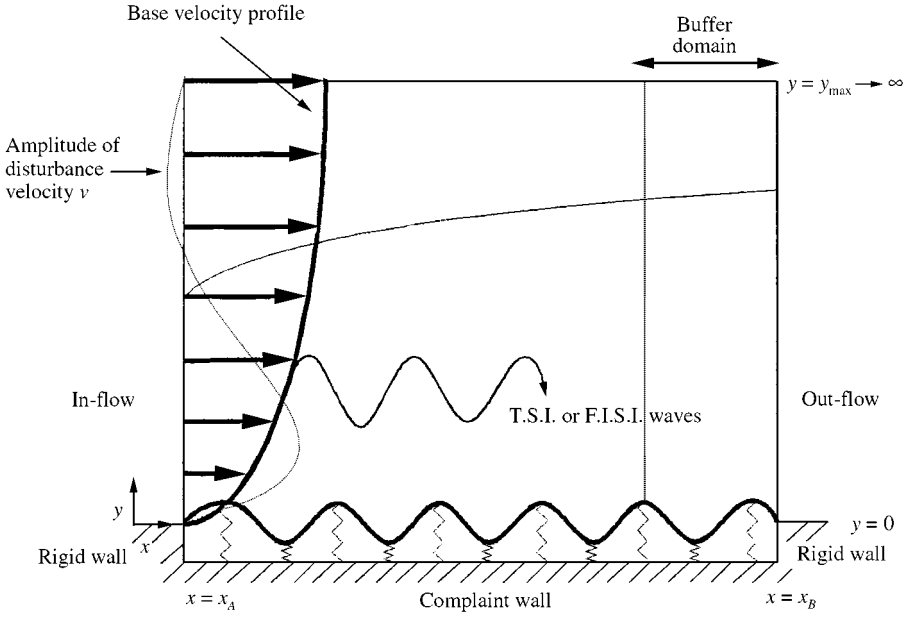

Figure 4. Sketch of the spatial computational domain.

be decomposed into modes, once the flow field has been obtained. For the streamwise component (as well as for the wall-normal component) one may write

$$u(x, y, t) = \sum_{n=0}^{\infty} u_{n1}(x, y)\sin(n\omega_0 t) + u_{n2}(x, y)\cos(n\omega_0 t). \tag{21}$$

Injecting the time-periodic disturbance at in-flow, for computations using the linearized Navier–Stokes system only the fundamental mode is nonzero. To compare the results with locally parallel, linear stability analysis, for this simulation the leading and the trailing edge of the compliant wall coincide, respectively, with the in-flow and out-flow of the computational domain; hence finite-length effects are minimized. The compliant-wall eigenmode provides the disturbance velocity profile (20) at in-flow x_a. Hinged-end conditions $\eta = \eta'' = 0$ at in-flow and out-flow are used in the dynamical equation (14). Although linear stability analyses predict non-zero values of η and η'', the homogeneous boundary conditions are easier to implement in the numerical solution procedure, the wall displacement and its derivatives appearing in the Navier-Stokes system as a consequence of the mapping (5).

The amplitude growth of the fundamental mode, the maximum being taken with respect to y for each x-location, is shown in Figure 5 as the solid line, whereas the amplitude growth predicted by the locally parallel, linear stability analysis is depicted as the broken line. In this linear case, the amplitude has been normalized to be equal to one at in-flow. After the wave has reached the out-flow of the whole domain, the modes are extracted from the flow field, following the simulation and integrating the convenient quantities over one period. In this and all subsequent figures the in-flow corresponds to $x = 0$. The curves coincide up to a certain x-location and then they diverge, nonparallelism leading to higher spatial growth rates. This is in qualitative agreement with the findings of Yeo *et al.* (1994), who showed that nonparallelism has an overall destabilizing influence on the Tollmien–Schlichting instabilities. The computation has been performed using 60 collocation points in the wall-normal direction. The stretching factor L in equation (15) is equal to 1, with $y_{\max} = 75$. The length of the physical domain is about $15\lambda_{TS}$ (λ_{TS} being the Tollmien–Schlichting wavelength). For space discretization 20 points per Tollmien–Schlichting wavelength have been used. The

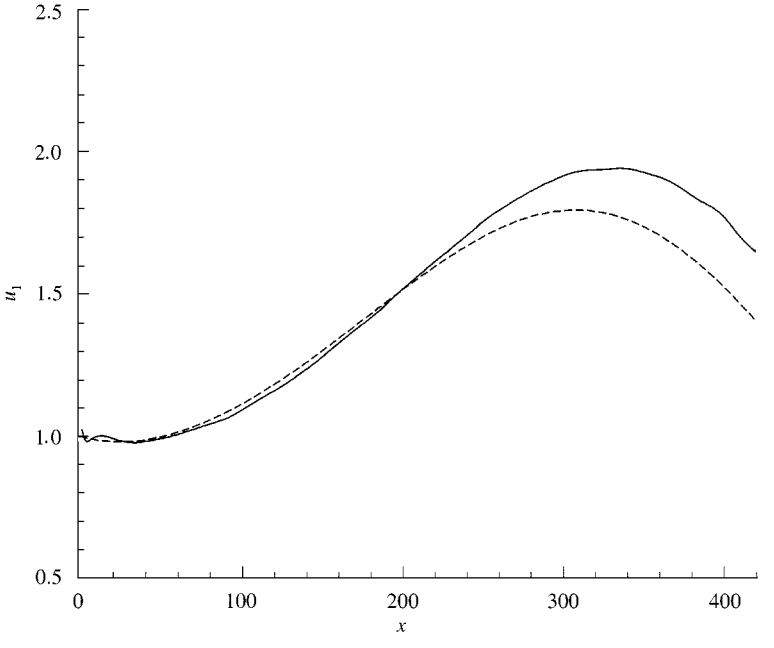

Figure 5. u_1 = maximum with respect to y of amplitude for fundamental mode of streamwise disturbance velocity: ——, linear spatial computation, for $t > 18\Lambda$: – – –, linear growth predicted by locally parallel linear stability analysis.

solution has been advanced in time with a time-step $\Delta t = 0{\cdot}1$. The buffer domain used here has a length of $3\lambda_{TS}$.

Solving now the full *nonlinear* two-dimensional Navier-Stokes system, an initial amplitude of $A = 0{\cdot}01$ has been considered in equation (20). The fundamental mode (the maximum with respect to y being taken for each x-location) for the compliant case is compared in Figure 6 to a rigid-wall computation, for the same frequency and inflow Reynolds number. It is interesting to note that the nonlinearities, although weak, affect the disturbance amplitudes which are decreased in the presence of the flexible boundary. The corresponding linear amplitude growth for the compliant-coating case, shown as the dotted line, is depicted as well, the initial amplitude being normalized for the curves to coincide at in-flow. One may expect a singular behaviour at in-flow due to the use of a hinged-end condition for the wall, and indeed the amplitude in the compliant case exhibits a small oscillation in the vicinity of in-flow at $x = 0$. The wall displacement $\eta(x, t)$ at $t = 18\Lambda$ is shown in Figure 7, exhibiting as expected a sudden slope at inflow. The buffer domain starts at the vertical dotted line, and indeed the amplitude is forced to converge to zero, and thus reflections are avoided at out-flow. A buffer domain which suppresses the perturbation has also been used by Kloker *et al.* (1993) for numerical transition studies in boundary layers.

Strongly nonlinear computations for the fluid structure interaction available are based on simplifying assumptions such as the locally parallel flow approximation (Ehrenstein & Rossi 1996) or an inviscid-fluid flow model (Lucey *et al.* 1997a). Hence, in a further step to test the nonlinear results of our numerical solution procedure, we compare rigid-wall results with those published by Joslin *et al.* (1992), by considering an identical test-case. The computational domain starts at $\mathrm{Re} = 688{\cdot}315$ with $\omega_0 = 0{\cdot}05921$ in Figure 3. The end of the physical domain is shown by a second point at $\mathrm{Re} = 1636$. (The length of the physical domain is about $30\lambda_{TS}$, and a buffer domain with a length of $3\lambda_{TS}$ has been considered.) Compared to Joslin *et al.* (1992), we used a rather coarse grid in the streamwise direction (with approximately 20 points per TS wavelength that is about 700 points in the whole domain). In the wall-normal direction we have used 60 collocation points, whereas about 640 time-steps have been used per period Λ. As in Joslin *et al.* (1992) the stretching factor L in equation (15) has been set to 10 (with $y_{max} = 75$).

The amplitude of the fundamental mode for the initial amplitude $A = 0{\cdot}0025$ (again for each x-location the maximum with respect to y has been taken) is shown in Figure 8. In order to facilitate the comparison we have extracted approximately the results of (Joslin *et al.* 1992, Figure 8) as data points. While the results almost coincide up to $x \approx 700$, the overall maximum peak is underestimated in our simulation. The amplitudes of the mean-flow distortion u_0 and the first harmonic u_2 are shown in Figure 9. Whereas the qualitative behaviour is the same as in Joslin *et al.* (in particular the cusp in the amplitude of the mean-flow distortion nearby $x = 750$ is captured), the maximum amplitudes are a factor of almost 2 lower in our simulation and any quantitative comparison is not meaningful. A grid refinement, using 40 points per TS wavelength in the streamwise direction, led to almost identical results (not plotted here). This indicates that the quantitative differences between the results of Joslin *et al.* and ours are not only due to the rather coarse grid we used. One may speculate, whether the discrepancy may also be a consequence of the different treatment in the buffer domain. While in Joslin *et al.* the Navier-Stokes system is continuously transformed into the (parabolic) boundary-layer equations, we transform the nonlinear Navier-Stokes system into a linear Stokes system. The latter procedure is compatible with the influence matrix technique we use to determine a Dirichlet boundary condition for the pressure, equivalent to the incompressibility condition. This procedure proved to be sufficiently robust to avoid reflections at out-flow in the coupled fluid–structure system. However, this transformation, smoothing out the perturbation in the buffer

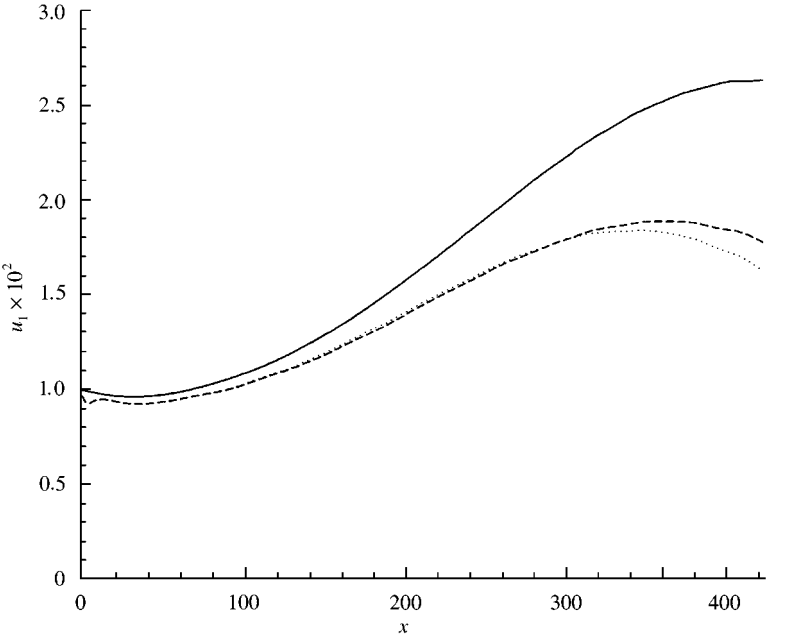

Figure 6. u = maximum with respect to y of amplitude for fundamental mode of streamwise disturbance velocity. Weakly nonlinear ($A = 0{\cdot}01$) spatial computation, for $t > 18\Lambda$: – – –, compliant case; —, rigid case; ····, linear spatial computation.

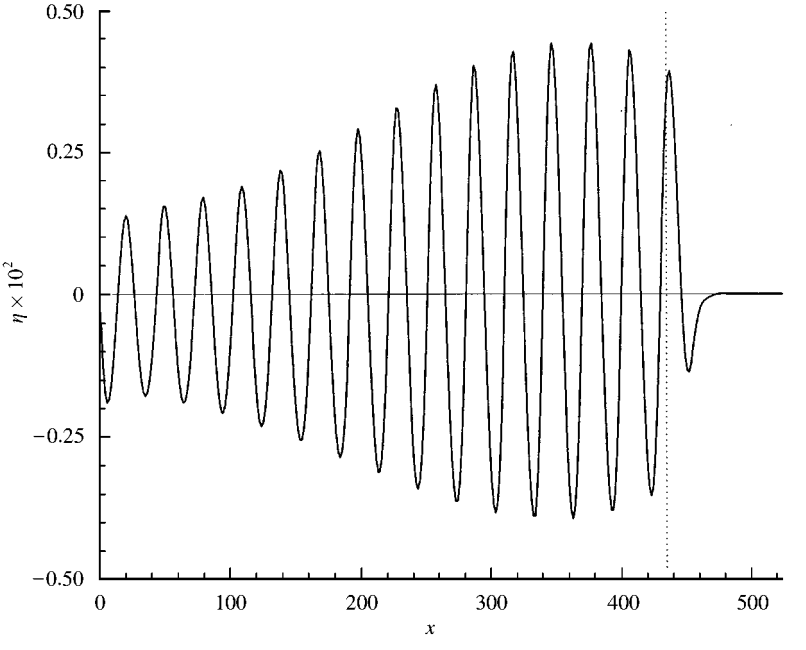

Figure 7. Spatial nonlinear evolution of wall displacement η at $t = 18\Lambda$, starting from $\otimes$ at Re = 600, $\omega = 0{\cdot}08$ in Figure 3, $A = 0{\cdot}01$. .... marks the end of the physical domain.

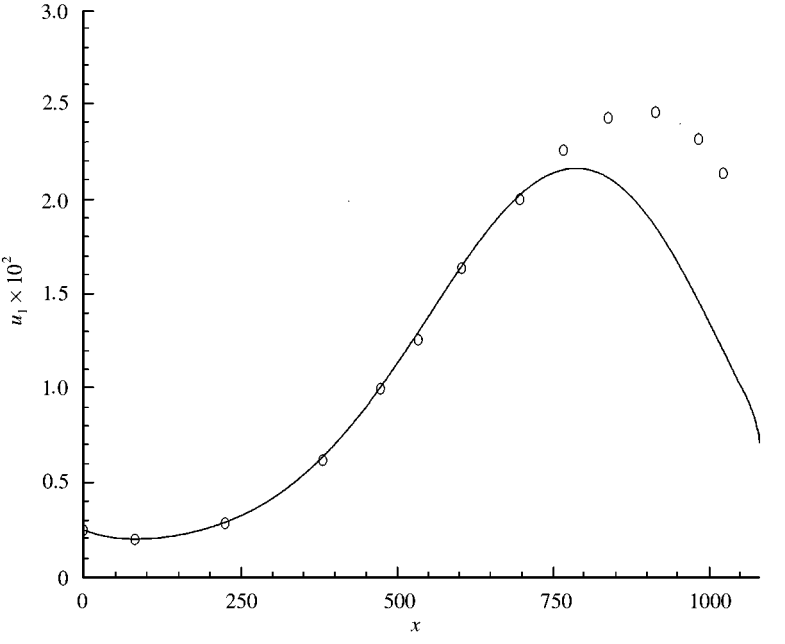

Figure 8. u_1 = maximum with respect to y of amplitude for fundamental mode of streamwise disturbance velocity, rigid case at $t > 33\Lambda$, with $A = 0{\cdot}0025$, starting from $\otimes$ at Re = 688·315 and $\omega = 0{\cdot}05921$ in Figure 3; $\bigcirc$: data points extracted from Joslin *et al.* (1992, Figure 8).

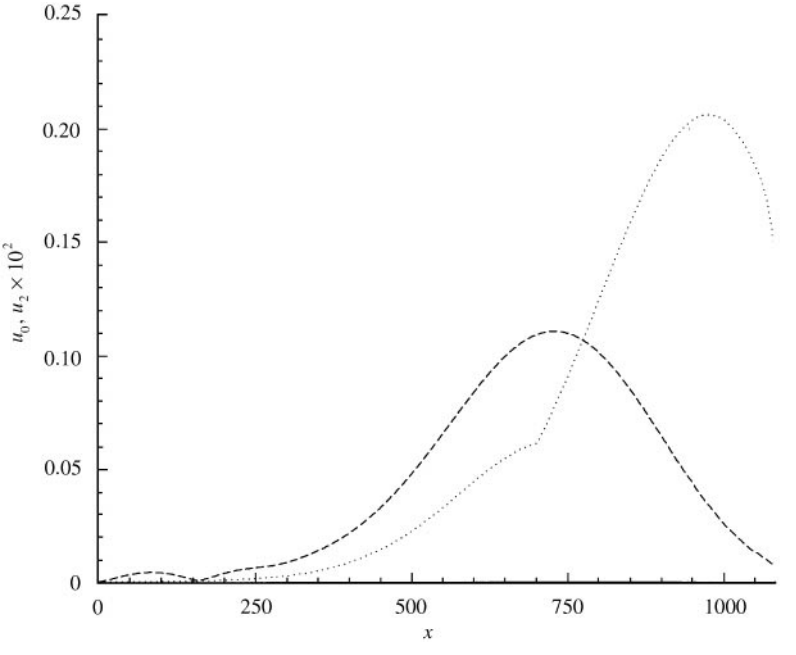

Figure 9. Rigid case starting from $\otimes$ at Re = 688·315 in Figure 3 with $A = 0{\cdot}0025$: ...., u_0 = maximum with respect to y of amplitude for mean-flow distortion; – – –, u_2 = maximum with respect to y of amplitude for first harmonic of streamwise disturbance velocity.

domain, may affect the nonlinear amplitudes upstream, while reproducing the qualitative behaviour.

Concluding the comparisons for the rigid-wall case, the trends of the nonlinear disturbance evolution are reproduced by our solution procedure, and the trends in the fluid–structure system are what we are focusing on in this paper. We have performed the same computations with a stretching factor $L = 1$ and we obtained the same results, except for some small oscillations near the out-flow of the physical domain. For our compliant-wall computations a stretching factor of $L = 1$ should be appropriate by distributing the collocation points closer to the wall rather than using higher values of L. The subsequent computations have been performed using about 20 points per wavelength in x and 60 collocation points in y. For time integration, in general a time step of 0·1 has been used.

3.3. Tensioned Membrane with Damping

In a previous paper (Ehrenstein & Rossi 1996) nonlinear Tollmien–Schlichting waves for a Blasius flow over compliant coatings have been computed, using a locally parallel flow assumption. For a certain class of compliant coatings, modelled as a tensioned membrane with damping, the nonlinear behaviour was shown to be subcritical. Here we take the same coating characteristics as in Ehrenstein & Rossi (1996) and the dimensionless parameter values in equation (2c) are defined as in Domaradzki & Metcalfe (1987), using reference values at x_0^* and hence Re_0 with

$$m = m_0 \mathrm{Re}_0/\mathrm{Re}, \quad d = d_0, \quad T = T_0 \mathrm{Re}_0/\mathrm{Re}\ (B = \kappa = 0).$$

[Indeed, in (2c) δ_a^* may be written as function of Re.] For $\mathrm{Re}_0 = 580$, $d_0 = 0{\cdot}2$ $m_0 = 0{\cdot}0212$, $T_0 = 15$, which are the parameter values used in Ehrenstein & Rossi (1996), the spatial linear stability results are depicted in Figure 10; the broken curve corresponds to the

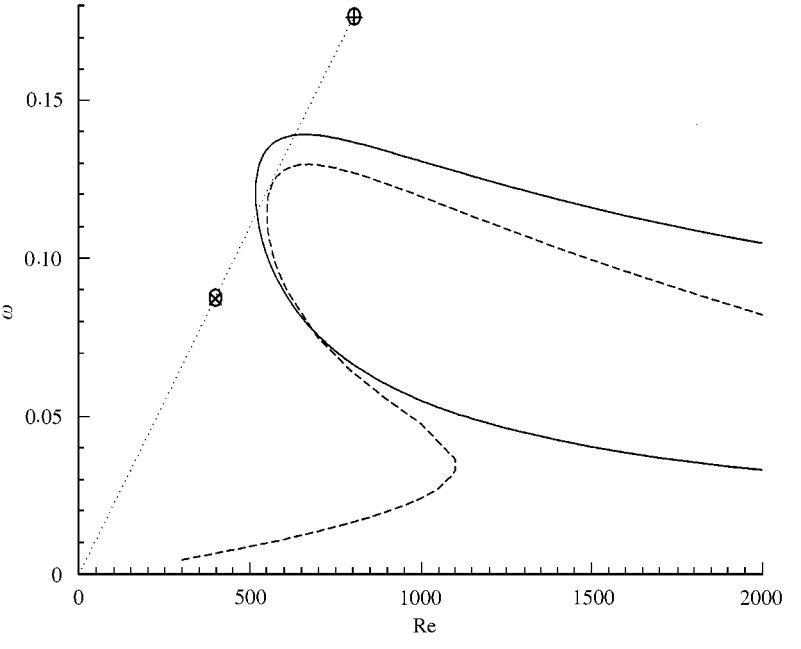

Figure 10. Neutral curves for spatial linear instability: —, rigid case; – – –, tensioned membrane with damping, $m_0 = 0{\cdot}0212$, $d_0 = 0{\cdot}2$, $T_0 = 15$, $\mathrm{Re}_0 = 580$. In-flow: ⊗ at Re = 400. Out-flow: ⊗ at Re = 807.

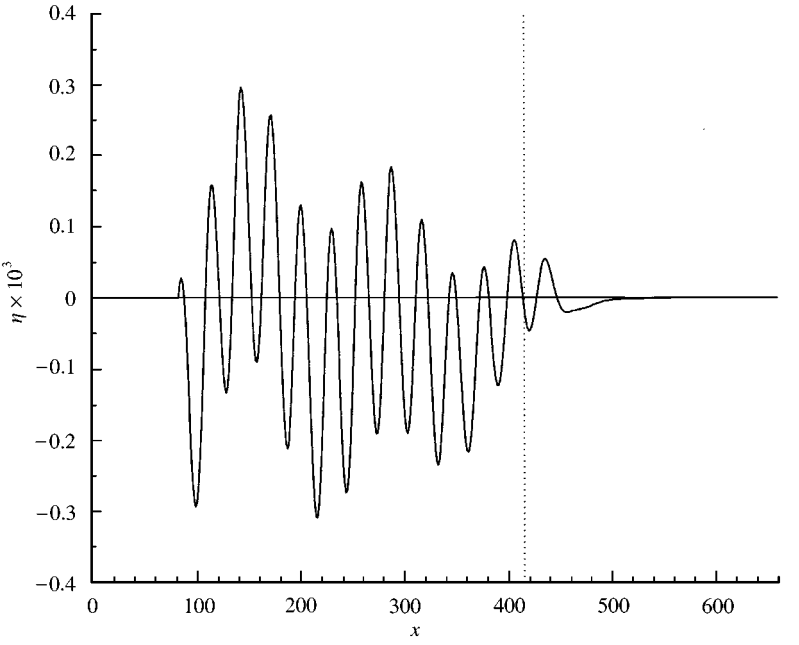

Figure 11. Tensioned membrane, spatial nonlinear evolution at $t = 24\Lambda$ of wall displacement η, starting from $\otimes$ at Re = 400 in Figure 10. Initial amplitude $A = 0{\cdot}001$; ...., end of physical domain.

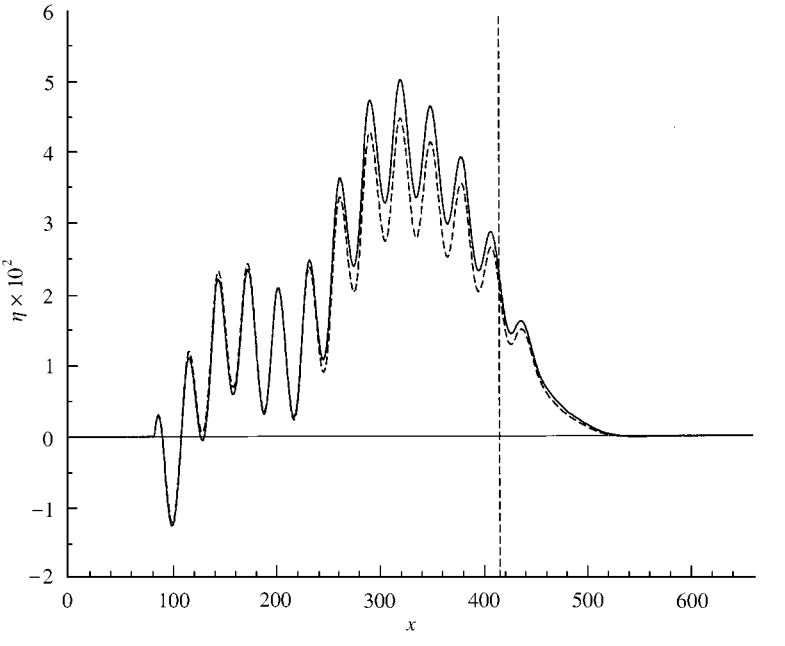

Figure 12. Tensioned membrane, spatial nonlinear evolution of wall displacement η, starting from $\otimes$ at Re = 400 in Figure 10. Initial amplitude $A = 0{\cdot}05$. – – –, at $t = 24\Lambda$; —, at $t = 25\Lambda$. Buffer domain starts at vertical line – – –.

compliant case. The in-flow for the spatial numerical simulation is located at $\mathrm{Re} = 400$ in the subcritical region and the frequency $\omega_0 = 0{\cdot}08756$ has been chosen such that the line passing through (0, 0) and (Re, ω_0) is tangent to the nose of the neutral curve. The inlet of the computational domain is located upstream of the membrane, that is a rigid wall with a length approximately equal to $3\lambda_{TS}$ has been inserted between the in-flow of the domain and the leading edge of the membrane. To avoid numerical difficulties for this numerical experiment however, the trailing edge of the membrane coincides with the computational out-flow boundary. The physical domain ends at $\mathrm{Re} = 807$, and in order to obtain reliable results we had to consider a rather long buffer domain with a length of $9\lambda_{TS}$ (the total computational domain having a length of $24\lambda_{TS}$). The nonlinear spatial development has been computed for the amplitudes $A = 0{\cdot}001$ and $A = 0{\cdot}05$ in equation (20), the in-flow disturbance being the rigid-wall Tollmien–Schlichting profile.

The wall displacement for an initial disturbance amplitude $A = 0{\cdot}001$ is shown in Figure 11, at $t = 24\Lambda$. The buffer domain starts at $x = 420$ (at approximately 15 wavelengths from in-flow). The leading edge of the tensioned membrane is located at $x = 80$, the boundary condition being $\eta = 0$ at the leading edge (as well as at the trailing edge at out-flow). The wall displacement exhibits a very sharp gradient at the leading edge. Besides the Tollmien–Schlichting instability, there is some evidence for the presence of a surface wave. For a higher initial disturbance amplitude, $A = 0{\cdot}05$, a quite different wall displacement is shown in Figure 12. The solutions at two different time periods ($t = 24\Lambda$ and 25Λ) almost superimpose, but now the membrane exhibits an overall deformed state. For this nonlinear computation the spatial evolution of the flow field, although dominated by the Tollmien–Schlichting instability, appears to be slightly affected by the overall buckling-like state of the surface, as depicted in Figure 13, where the maximum with respect to y of the streamwise disturbance velocity is shown. The amplitudes of the fundamental

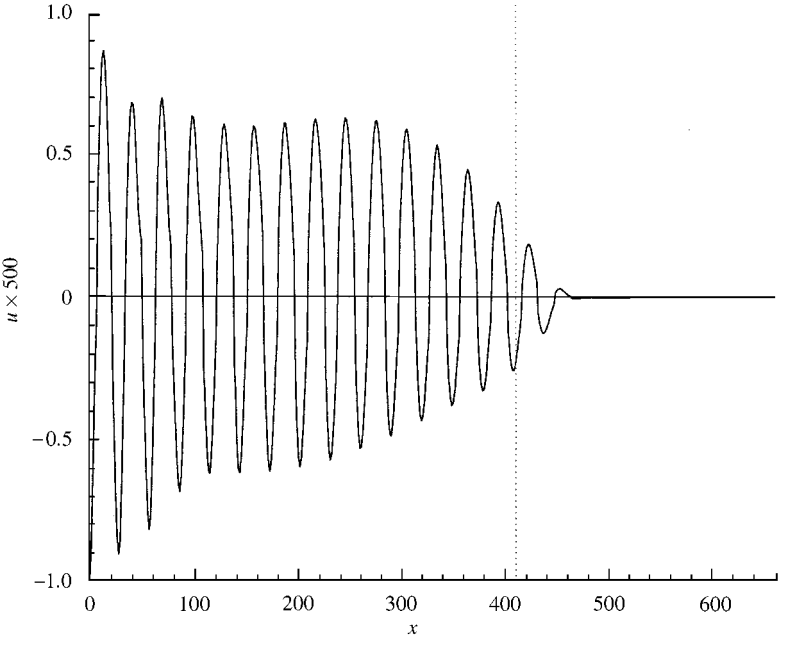

Figure 13. Tensional membrane $\max_y u(x, y)$ of streamwise disturbance velocity, $A = 0{\cdot}05$, at $t = 24\Lambda$, starting from $\otimes$ at $\mathrm{Re} = 400$ in Figure 10; ....: end of physical domain.

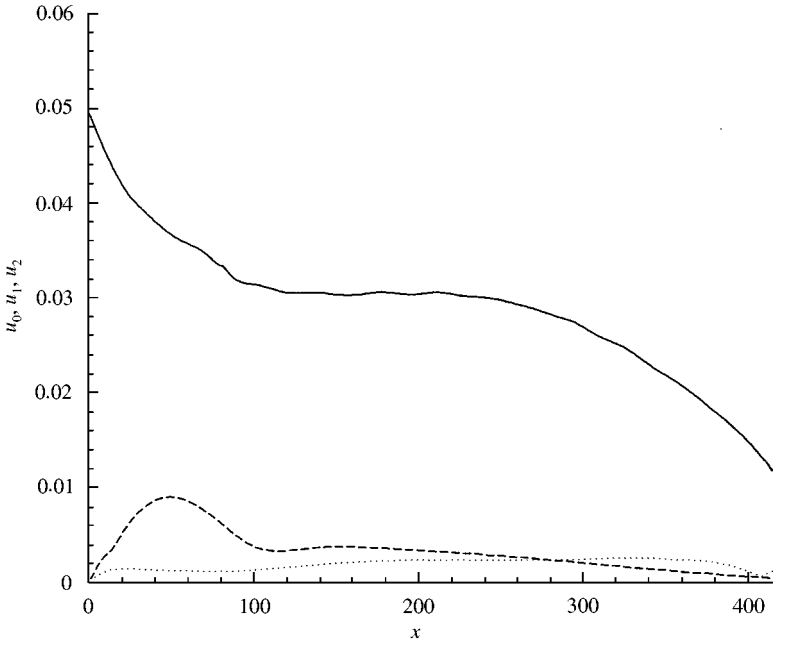

Figure 14. Tensioned membrane, maximum with respect to y of amplitude for streamwise disturbance velocity modes, $A = 0{\cdot}05$, $t > 24\Lambda$: ...., u_0; —, u_1; – – –, u_2.

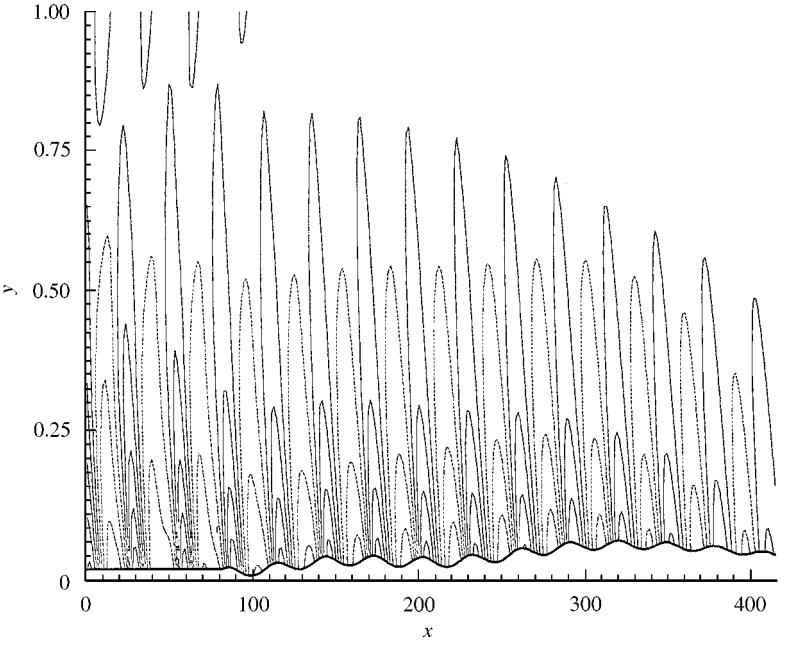

Figure 15. Isolines of disturbance vorticity over tensioned membrane, with initial amplitude $A = 0{\cdot}05$, at $t = 24\Lambda$.

mode u_1, of the mean-flow distortion u_0 and of the first harmonic u_2 (as function of x, the maximum being taken with respect to y) are shown in Figure 14. Whereas the amplitudes vary only slightly for $100 < x < 300$, the perturbation ultimately decreases when reaching the boundary of the physical domain (at $\mathrm{Re} = 807$ in Figure 10). Finally, a global picture of the flow for this last case (at $t = 24\Lambda$) is given in Figure 15, where the isolines of the disturbance flow vorticity are shown, in the physical coordinates (x, y). The surface motion clearly affects the flow field, and the overall deformation is not negligible any more (here $y = 1$ corresponds to the displacement thickness).

Even though the computational domain is perhaps not large enough in the streamwise direction, there is nevertheless evidence that nonlinearities strongly affect the waveform of the surface instability. With the present computational facilities available it would hardly be possible to substantially increase the spatial domain. Indeed, the numerical algorithm to solve the full nonlinear system (10)–(14) is rather time-consuming. At each time-step the non-Cartesian parts (6c)–(6e) of the operators have to be computed, which increases substantially the CPU-time. The computations have been performed on a 128 Mbyte workstation Digital Alpha 200 4/166, and one run with 24 Tollmien–Schlichting wavelengths (with 480 point in x and 60 collocation points in y, with about $1{\cdot}8 \times 10^4$ time-steps) necessitates about 48 h on the workstation. Using one processor of the IBM/SP2 of the CNUSC, France, about 10 h were necessary.

3.4. Spring-Backed Elastic Plate of Finite Length

Again, we consider a spring-backed elastic plate with the same wall characteristics as those of Section 3.1 (with an elastic modulus of $E = 0{\cdot}5\ \mathrm{MN/m^2}$, spring stiffness $\kappa^* = 115\ \mathrm{MN/m^3}$, plate density $\rho_m = 946\ \mathrm{kg/m^3}$, and plate thickness $b = 2\ \mathrm{mm}$, the fluid

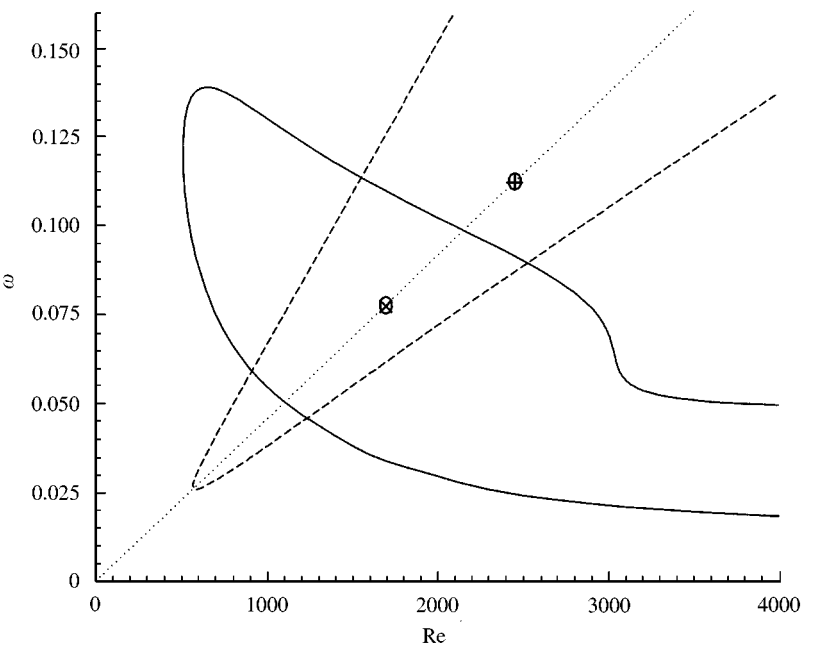

Figure 16. Neutral curves, spatial linear stability for spring-backed elastic plate with $b = 2\ \mathrm{mm}$, $E = 0{\cdot}5\ \mathrm{MN/m^2}$ and $\kappa^* = 115\ \mathrm{MN/m^3}$: —, Tollmien–Schlichting instabilities; – – –, flow-induced surface instabilities. In-flow: ⊗ at $\mathrm{Re} = 1700$; out-flow: ⊗ at $\mathrm{Re} = 2460$.

being water with $U_\infty^* = 18$ m/s). The linear stability results are depicted in Figure 16 and, besides the Tollmien–Schlichting instabilities, flow-induced surface instabilities are now present. Linear stability computations for similar compliant coatings have been reviewed for instance by Carpenter (1990). In some cases, the neutral curve for Tollmien–Schlichting waves splits into two disconnected curves for increasing Reynolds number. This may be explained by considering the dependence of the dimensionless coating parameters (2c) on the reference length δ^*, which in fact depends on Reynolds number Re in the locally parallel flow assumption used for the linear stability analysis. For instance, κ increases with Re, whereas B decreases with Re^3. Now, as shown by Carpenter (1990) among others, for sufficiently flexible coatings (for example by use of a small plate thickness) Tollmien–Schlichting waves may be suppressed for a certain range of Re-values before appearing again for increasing Re [due to a (dimensionless) spring stiffness increase, for instance]. While the region of instability is still connected in the present case, the kink in the upper branch of the neutral curve for Tollmien–Schlichting waves in Figure 16 illustrates that the curve may be disconnected for slightly different coating characteristics.

As shown by the broken curve in Figure 16, besides the Tollmien–Schlichting instability, flow-induced surface instabilities are also present. Inspecting the dynamical equation (2a), in the present case free waves even in the absence of pressure forcing may exist. In the absence of external forcing, a solution $\eta = \Re(\eta_p(x)\mathrm{e}^{\mathrm{i}\omega t})$ of equation (2a) exists for $\omega^2 m - \kappa > 0$ and then $\eta_p(x) = \sin(\beta x)$ with $\beta = [(\omega^2 m - \kappa)/B]^{1/4}$. For the coating parameters considered here with a perturbation frequency $\omega_0 = 0{\cdot}078$ at the point marked at $\mathrm{Re} = 1700$ in Figure 16, one finds $\beta = 0{\cdot}0914$. When fluid flow is present, the solution is modified and a flow-induced surface instability may be observed [cf. Davies & Carpenter (1997a)]. The *spatial* stability computation for the same frequency and Reynolds number predicts three instability modes with complex wave numbers

$$\alpha_1 = 0{\cdot}0932 - \mathrm{i}0{\cdot}0001536, \quad \alpha_2 = 0{\cdot}143 - \mathrm{i}0{\cdot}001012, \quad \alpha_3 = 0{\cdot}237 - \mathrm{i}0{\cdot}01016.$$

The first wave number corresponds to the free-wave mode, the second one is again a flow-induced surface instability and the third one is the complex wave number associated to the Tollmien–Schlichting instability.

In order to simulate a true physical experiment a panel of finite length has been considered, the leading edge being located at a distance of $3\lambda_{\mathrm{TS}}$ from in-flow and adjacent to the trailing edge there is again a rigid plate with length equal to $6\lambda_{\mathrm{TS}}$. The compliant panel has a length of $15\lambda_{\mathrm{TS}}$ with $\lambda_{\mathrm{TS}} = 26{\cdot}5$. The free-wave mode wavelength is about 2·5 times larger than λ_{TS}, and this may affect the length of the buffer domain, for a semi-infinite compliant panel. However, for the present computation, a rigid plate is inserted between the compliant panel and the end of the physical domain. Hence, the flow disturbance at the end of the physical domain will be dominated by the Tollmien–Schlichting instability, and a buffer domain of length $3\lambda_{\mathrm{TS}}$ has proved to be sufficient to avoid reflections at outflow. The whole computational domain has an overall length of approximately $27\lambda_{\mathrm{TS}}$. Rather than hinged-end conditions, which would lead to a discontinuous first derivative of the wall displacement η at the leading and trailing edge, we used clamped-end conditions where η and $\partial\eta/\partial x$ are set equal to zero at the panel ends. Our solution procedure is based on a variable transformation leading to various terms in the momentum equations depending on the wall displacement, which necessitates some regularity of η.

The spatial simulation starts at the point marked at $\mathrm{Re} = 1700$ in Figure 16 and the physical domain ends at the second point marked at $\mathrm{Re} = 2460$. Using the full nonlinear system, an initial amplitude $A = 0{\cdot}001$ has been considered at in-flow. Simulations using the linearized system have been performed as well, for comparison. The instantaneous wall displacement at $t = 27\Lambda$ is shown in Figure 17. For both the linear and nonlinear

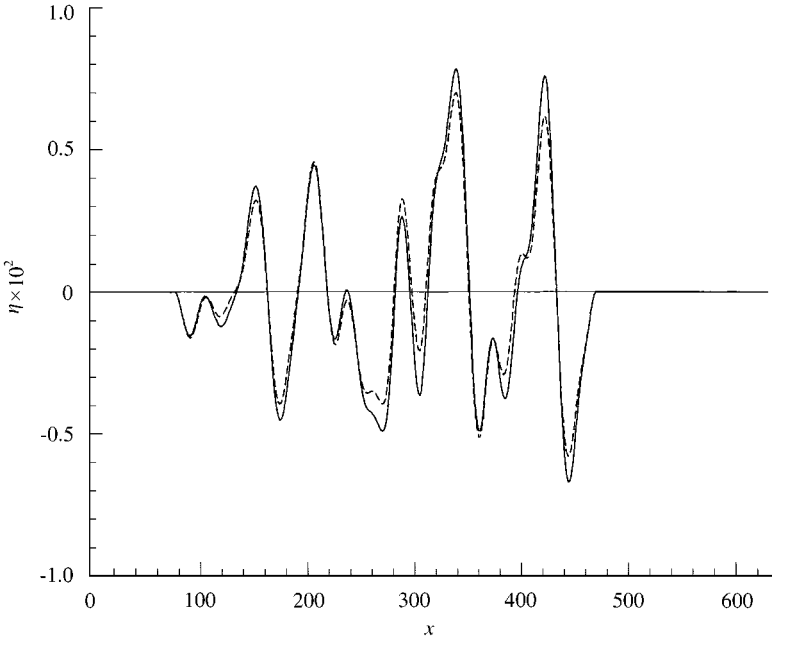

Figure 17. Elastic plate, spatial nonlinear evolution at $t = 27\Lambda$ of wall displacement η, starting from $\otimes$ at Re = 1700 in Figure 16: —, nonlinear computation, initial amplitude $A = 0{\cdot}001$; – – –, linear computation.

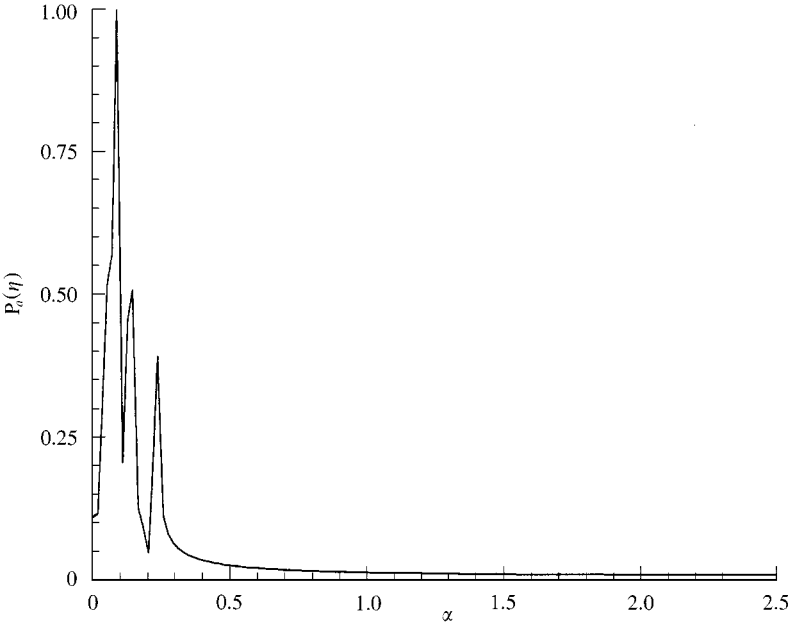

Figure 18. Elastic plate, power spectrum for wall displacement depicted in Figure 17.

computations the wall displacement exhibits an interaction between the different instability modes, the boundary being flat at the rigid parts adjacent to each side of the compliant panel. A discrete Fourier transform has been taken of the wall displacement (the solid line in

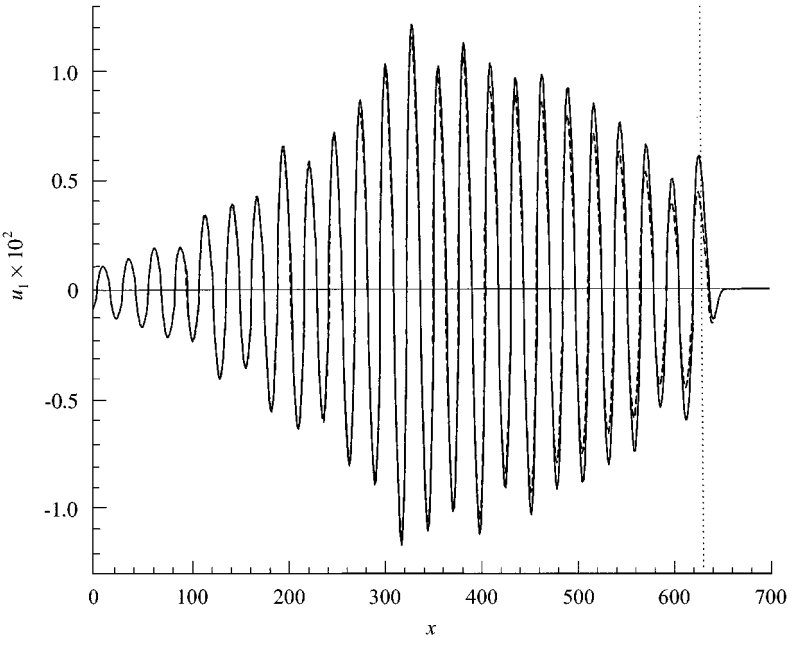

Figure 19. Elastic plate, $\max_y u(x, y)$ of streamwise disturbance velocity, at $t = 27\Lambda$, starting from $\otimes$ at Re = 1700 in Figure 16: —, nonlinear computation, initial amplitude $A = 0{\cdot}001$; – – –, linear computation. ....: End of physical domain.

Figure 17) and the power spectrum is depicted in Figure 18. It is clearly seen that there are three components corresponding respectively to the three real parts of the spatial eigenvalues α_1, α_2 and α_3. The maximum with respect to y of the streamwise component of the disturbance velocity is depicted in Figure 19, at $t = 27\Lambda$. The instability of the fluid flow is clearly dominated by the Tollmien–Schlichting wave, and again the disturbance is suppressed in the buffer domain. A comparison with the linear results, plotted as a broken line, shows that for an amplitude at in-flow of $A = 0.001$ the nonlinearities only slightly affect the overall disturbance amplitude. The end of the physical domain being outside the unstable region (cf. Figure 16), the amplitude ultimately decays in the physical domain.

4. SUMMARY

A computational method has been developed in order to study the spatial evolution of disturbances in a boundary layer with compliant coatings. The method takes into account the full nonlinear fluid-structure interaction as well as nonparallelisms due to the wall displacement and to the boundary-layer growth.

The method is capable of reproducing the spatial evolution of Tollmien–Schlichting-type waves, in the linear and nonlinear regime. Computations of linear disturbance evolution confirm that the inclusion of terms due to nonparallel effects leads to higher disturbances amplitudes.

Concerning the nonlinear disturbance evolution, a tensioned membrane has been considered. Using a locally parallel flow assumption, nonlinear travelling waves have been computed in the past by Ehrenstein & Rossi (1996) in subcritical parameter regions. For the physically more realistic numerical experiment reported in the present paper, even for initial

disturbance amplitudes triggering the nonlinear regime, the Tollmien–Schlichting type waves ultimately decay in the subcritical region. However, when strong nonlinearities are present, the compliant membrane with damping exhibits an overall deformed state, and the associated instability mechanism is not of travelling-wave type. The influence of nonlinearities on the deformation of damped coatings has been assessed recently by Lucey *et al.* (1997a), who focus on a nonlinear panel model driven by nonlinear perturbation pressure resulting from unsteady potential flow. While the present computations indicate that the observed divergence-type behaviour depends on the nonlinearities, the importance of this phenomenon has to be confirmed by further numerical experiments.

A physically realistic numerical experiment has been performed by considering a spring backed elastic plate of finite length. A highly unstable parameter region has been considered and it has been shown that the model is capable of reproducing the different instability mechanisms present in this coupled fluid-structure system.

Concluding, the computational model presented in this paper appears to be a numerical tool suitable for studying the influence of compliant coatings on instabilities in boundary-layer flow. Here we have only considered a two-dimensional flow-field, focusing on the complex geometry depending on the streamwise direction and on time. If one supposes the geometry to be homogeneous in a third, spanwise direction, one may expand the flow quantities in a Fourier series in the spanwise coordinate. The solution procedure described in the present paper may then be adapted to solve the system for each Fourier mode, and the numerical method used here may be the starting point for forthcoming developments.

ACKNOWLEDGMENTS

This work has been supported by the DGA, Direction des Systèmes de Force et de la Prospective, France (Contract ERS No. 97, 1046A./DSP). Parts of the computations have been performed on the IBM/SP2 of the CNUSC, France. Also the constructive criticism of the referees is gratefully acknowledged.

References

Benjamin, T. B. 1960 Effects of a flexible boundary on hydrodynamic stability. *Journal of Fluid Mechanics* **9,** 513–532.

Canuto, C., Hussaini, A., Quarteroni, A. & Zang, T. A. 1987 *Spectral Methods in Fluid Dynamics*. New York: Springer Series in Computational Physics.

Carlson, H. A., Berkooz, G. & Lumley, J. L. 1995 Direct numerical simulation of flow in a channel with complex, time-dependent wall geometries: a pseudospectral method. *Journal of Computational Physics* **121,** 155–175.

Carpenter, P. W. 1990 Status of transition delay using compliant walls. In *Viscous Drag Reduction in Boundary Layers*, Progress in Astronautics and Aeronautics (eds D. M. Bushnell & J. N. Hefer) **123,** 79–113. New York: AIAA.

Carpenter, P. W. & Gajjar, J. S. B. 1990 A general theory for two- and three- dimensional wall-mode instabilities in boundary-layer over isotropic and anisotropic compliant walls. *Theoretical and Computational Fluid Dynamics* **1,** 349–378.

Carpenter, P. W. & Garrad, A. D. 1985 The hydrodynamic stability of flow over Kramer-type compliant surfaces. Part 1. Tollmien–Schlichting instabilities. *Journal of Fluid Mechanics* **155,** 465–510.

Carpenter, P. W. & Garrad, A. D. 1986 The hydrodynamic stability of flow over Kramer-type compliant surfaces. Part 2. Flow-induced surface instabilities. *Journal of Fluid Mechanics* **170,** 199–232.

Davies, C. & Carpenter, P. W. 1997a Numerical simulation of the evolution of Tollmien–Schlichting waves over finite compliant panels. *Journal of Fluid Mechanics* **335,** 361–392.

Davies, C. & Carpenter, P. W. 1997b Instabilities in a plane channel flow between compliant walls. *Journal of Fluid Mechanics* **352,** 205–243.

Deissler, R. J. 1987 The convective nature of instability in plane Poiseuille flow. *Physics of Fluids* **30,** 2303–2305.

Domaradzki, J. A. & Metcalfe, R. E. 1987 Stabilization of laminar boundary layers by compliant membranes. *Physics of Fluids* **30,** 695–705.

Ehrenstein, U. & Peyret, R. 1989 A Chebyshev collocation method for the Navier–Stokes equations with application to double diffusive convection. *International Journal of Numerical Methods in Fluids* **9,** 427–452.

Ehrenstein, U. & Rossi, M. 1993 Nonlinear Tollmien–Schlichting waves for plane Poiseuille flow with compliant walls. *European Journal of Mechanics B/Fluids* **12,** 789–810.

Ehrenstein, U. & Rossi, M. 1996 Nonlinear Tollmien–Schlichting waves for a Blasius flow over compliant coatings. *Physics of Fluids* **8,** 1036–1051.

Gad-el-hak, M. 1986 Boundary-layer interactions with compliant coatings: an overview. *Applied Mechanics Reviews* **39,** 511–524.

Gad-el-hak, M. 1996 Compliant coatings: a decade of progress. *Applied Mechanics Reviews* **49,** S147–S157.

Gaster, M. 1987 Is the dolphin a red herring? In *IUTAM Symposium on Turbulence Management and Relaminarisation*, (eds H.W. Liepmann & R. Narasimha), pp. 285–304, New York: Springer.

Joslin, R. D. & Morris, P. J. 1989 The sensitivity of flow and surface instabilities to changes in compliant wall properties. *Journal of Fluids and Structures* **3,** 423–437.

Joslin, R. D. & Morris, P. J. 1992 Effect of compliant walls on secondary instabilities in boundary-layer transition. *AIAA Journal* **30,** 332–339.

Joslin, R. D., Streett, C. L. & Chang, C. L. 1992 Validation of three-dimensional incompressible spatial direct numerical simulation code–a comparison with linear stability and parabolic stability equation theories for boundary-layer transition on a flat plate. NASA TP-3205.

Joslin, R. D., Streett, C. L. & Chang, C. L. 1993 Spatial direct numerical simulation of boundary-layer transition mechanisms: validation of PSE theory. *Theoretical and Computational Fluid Dynamics* **4,** 271–288.

Kloker, M., Konzelmann, U. & Fasel, H. 1993 Outflow boundary conditions for spatial Navier–Stokes simulations of transition boundary layers. *AIAA Journal* **31,** 620–628.

Kramer, M. O. 1960 Boundary-layer stabilization by distributed damping. *Journal of the American Society of Naval Engineers* **72,** 25–33.

Lucey, A. D., Cafolla, G. J., Carpenter, P. W. & Yang, M. 1997a The nonlinear hydroelastic behaviour of flexible walls. *Journal of Fluids and Structures* **11,** 717–744.

Lucey, A. D., Cafolla, G. J. & Carpenter, P. W. 1997b Numerical simulation of a boundary-layer flow interacting with a compliant boundary. *Lecture Notes in Physics* **490,** 406–411.

Lucey, A. D., & Carpenter, P. W. 1995 Boundary layer instability over compliant walls: Comparison between theory and experiment. *Physics of Fluids* **7,** 2355–2363.

Metcalfe, R. W., Rutland, C. J., Duncan, J. H. & Riley, J. J. 1986 Numerical simulation of active stabilization of laminar boundary-layers. *AIAA Journal* **24,** 1494–1501.

Riley, J. R., Gad-el-hak, M. & Metcalfe, R. W. 1988 Compliant coatings. *Annual Review of Fluid Mechanics* **20,** 393–420.

Rist, U. & Fasel, H. 1995 Direct numerical simulation of controlled transition in a flat-plate boundary layer. *Journal of Fluid Mechanics* **298,** 211–248.

Rotenberry, J. M. 1992 Finite amplitude shear waves in a channel with compliant boundaries. *Physics of Fluids A* **4,** 270–276.

Schlichting, H. 1979 *Boundary-Layer Theory*, 7th edition New York: McGraw-Hill.

Streett, C. L. & Macareag, M. G. 1989 Spectral multi-domain for large-scale fluid dynamic simulations. *International Journal of Applied Numerical Mathematics* **6,** 123–140.

Thomas, M. D. 1992 The nonlinear stability of flows over compliant walls. *Journal of Fluid Mechanics* **239,** 657–670.

Yeo, K. S., Khoo, B. C. & Chong, W. K. 1994 The linear stability of boundary-layer flow over compliant walls: effects of boundary-layer growth. *Journal of Fluid Mechanics* **280,** 199–225.

APPENDIX: THE INFLUENCE MATRIX TECHNIQUE

At each time-step, system (10)–(14) has to be solved. In order to find a Dirichlet boundary condition for the pressure, equivalent to equation (12), one proceeds as follows (the technique is analogous to

that used for instance by Ehrenstein & Peyret (1989) for a vorticity-stream function formulation of the Navier-Stokes equations). Dropping the prime for the operators and the variables, the system (10)–(14) is formally written as

$$(\Delta - 3\sigma)\mathbf{u}^{n+1} = -\nabla q^{n+1} + \mathbf{f}^{n,n-1}, \tag{A1}$$

$$\Delta q^{n+1} = g^{n,n-1}, \tag{A2}$$

$$\nabla \cdot \mathbf{u}^{n+1} = h^{n,n-1} \quad \text{on the boundary } \Gamma, \tag{A3}$$

$$u^{n+1} = 0, \quad v^{n+1} = \alpha\eta^{n+1} + \eta^{n,n-1} \quad \text{a } y = 0, \tag{A4}$$

$$L\eta^{n+1} = \eta^{n,n-1} - p^{n+1} + \varphi^{n,n-1} \quad \text{at } y = 0, \tag{A5}$$

L being the differential operator of the dynamical equation (14) and $\eta^{n,n-1}$ are the explicit terms resulting from the time-differencing (and $q = \mathrm{Re}\, p$). (Note that u, v are zero at infinity, and equal to perturbation profiles at in-flow.) First, before starting the time integration, the following set of equations is solved:

$$\Delta\hat{q}_k = 0, \quad \hat{q}_k(\tau_i) = \delta_{ki},$$

with τ_i the ith point on the boundary Γ, and δ_{ki} being the Kronecker symbol.

Knowing $\hat{q}_k$, $1 \le k \le K$, K being the total number of points on the boundary (in-flow, compliant wall and out-flow, the perturbation pressure and velocity being zero at infinity), one computes

$$L\hat{\eta}_k = -\hat{p}_k \quad \text{and } (\Delta - 3\sigma)\hat{\mathbf{u}}_k = -\nabla\hat{q}_k,$$

with

$$\hat{u}_k = 0, \quad \hat{v}_k = \alpha\hat{\eta}_k \text{ at } y = 0; \quad \hat{u}_k = \hat{v}_k = 0 \text{ elsewhere on } \Gamma.$$

Knowing the elementary solutions, the columns of the influence matrix $\mathbf{M}$ are computed once and for all, with

$$M = [\nabla \cdot \hat{\mathbf{u}}_{1_{|\Gamma}}, \nabla \cdot \hat{\mathbf{u}}_{2_{|\Gamma}}, \ldots, \nabla \cdot \hat{\mathbf{u}}_{K_{|\Gamma}}],$$

each column vector $\nabla \cdot \hat{\mathbf{u}}_{j_{|\Gamma}}$ being evaluated at the points on the boundary.

During the time integration, at each time-step the following inhomogeneous problems are solved:

$$\Delta\tilde{q} = g^{n,n-1}, \quad \tilde{q}_{|\Gamma} = 0,$$

$$L\tilde{\eta} = \eta^{n,n-1} + \varphi^{n,n-1} \quad \text{at } y = 0,$$

$$(\Delta - 3\sigma)\tilde{\mathbf{u}} = -\nabla\tilde{q} + \mathbf{f}^{n,n-1},$$

$$\tilde{u} = 0, \quad \tilde{v} = \alpha\tilde{\eta} + \eta^{n,n-1} \quad \text{at } y = 0,$$

(+ inhomogeneous inflow conditions). The values of $\nabla \cdot \tilde{\mathbf{u}}$ at the boundary points are computed and the vector $\boldsymbol{\gamma}$ solution of

$$\mathbf{M}\boldsymbol{\gamma} = -\nabla \cdot \tilde{\mathbf{u}}_{|\Gamma} + h^{n,n-1}$$

contains the pressure values at the boundary points equivalent to equation (A3). Once the vector $\boldsymbol{\gamma}$ determined, equation (A2) is solved with $q^{n+1}(\tau_i) = \gamma_i$, $1 \le i \le K$, equivalent to equation (A3); then η is computed using equation (A5), and finally equation (A1) is solved with the kinematical conditions (A4).